Physics of the Earth and Planetary Interiors 180 (2010) 80–91

Contents lists available at ScienceDirect

Physics of the Earth and Planetary Interiors

journal homepage: www.elsevier.com/locate/pepi

Imaging the upper mantle transition zone with a generalized Radon transform of *SS* precursors

Q. Cao[a,*], P. Wang[a], R.D. van der Hilst[a], M.V. de Hoop[b], S.-H. Shim[a]

[a] Earth, Atmospheric, and Planetary Sciences, Massachusetts Inst. of Technology, Cambridge, MA 02139, USA
[b] Center for Computational and Applied Mathematics, Purdue University, West Lafayette, IN 47907, USA

ARTICLE INFO

Article history:
Received 2 February 2009
Received in revised form 9 February 2010
Accepted 9 February 2010

Edited by: G. Helffrich.

Keywords:
Transition zone
Upper mantle discontinuities
Inverse scattering
Generalized Radon transform
SS precursors

ABSTRACT

We demonstrate the feasibility of using inverse scattering for high-resolution imaging of discontinuities in the upper mantle beneath oceanic regions (far from sources and receivers) using broadband wavefield observations consisting of *SS* and its precursors. The generalized Radon transform (GRT) that we developed for this purpose detects (in the broadband data) signals due to scattering from elasticity contrasts in Earth's mantle. Synthetic tests with realistic source–receiver distributions demonstrate that the GRT is able to detect and image deep mantle interfaces, even in the presence of noise, depth phases ('ghosts'), phase conversions, and multiples generated by reverberation within the transition zone. As a proof of concept, we apply the GRT to ~50,000 broadband seismograms to delineate interfaces in the depth range from 300 to 1000 km beneath the northwest Pacific. We account for smooth 3D mantle heterogeneity using first-order perturbation theory and independently obtained global tomography models. The preliminary results reveal laterally continuous (but undulating) scatter zones near 410 and 660 km depth and a weaker, broader, and more complex structure near 520 km depth. The images also suggest the presence of multiple, laterally intermittent interfaces near 350 km and between 800 and 1000 km depth, that is, above and below the transition zone *sensu stricto*. Filtering of the data (we consider four pass-bands: 20–50 s, 10–50 s, 5–50 s, and 2–50 s) reveals a prominent frequency dependence of the magnitude, width, and complexity of the interfaces, in particular of the scatter zone near 520 km depth; such dependencies may put important constraints on the mineralogy and phase chemistry of the transition zone.

1. Introduction

The upper mantle transition zone, here taken broadly as the depth interval between 300 and 1000 km depth, is marked by rapid radial changes in elasticity and mass density associated with phase transformations in mantle silicates (Fig. 1) (e.g., Ringwood, 1975; Weidner and Wang, 2000; Li and Liebermann, 2007). With seismic imaging one can estimate the depth to and the change in elasticity and mass density across such phase boundaries. Combined with mineral physics data this information puts constraints on local temperature, composition, and mineral phase, and the geographic variation of these parameters provides insight into large-scale geodynamical processes (Jeanloz and Thompson, 1983; Helffrich, 2000; Shearer, 2000; Weidner and Wang, 2000; Schmerr and Garnero, 2006; Li and Liebermann, 2007).

Using a variety of top- and underside reflections and phase-converted waves, a number of seismic investigations have observed the global existence of what are usually referred to as '410' and '660' discontinuities (e.g., Shearer and Masters, 1992; Shearer, 1993; Gossler and Kind, 1996; Flanagan and Shearer, 1998a,b; Gu et al., 1998; Flanagan and Shearer, 1999; Gu and Dziewonski, 2002; Lebedev et al., 2002, 2003; Chambers et al., 2005a,b; Deuss et al., 2006; Schmerr and Garnero, 2006; An et al., 2007; Rost and Thomas, 2009), and a '520' discontinuity has been reported in some regions (e.g., Shearer, 1990; Deuss and Woodhouse, 2001). Many aspects of these discontinuities can be explained by phase transitions in the olivine system (olivine to wadsleyite, wadsleyite to ringwoodite, and ringwoodite to perovskite and ferropericlase, respectively) (Ringwood, 1969, 1975, 1991; Katsura and Ito, 1989; Bina and Helffrich, 1994; Shim et al., 2001; Lebedev et al., 2002, 2003; Fei et al., 2004; Weidner and Wang, 2000; Weidner et al., 2005; Li and Liebermann, 2007), but not all seismic observations are consistent with transformations in a simple, isolated $MgO–FeO–SiO_2$ system. For example, despite the opposite signs of their Clapeyron slopes, on a global scale the '410' and '660' topographies are not convincingly anti-correlated (Gu et al., 1998, 2003;

---

* Corresponding author at: Massachusetts Inst. of Technology, Earth, Atmospheric, and Planetary Sciences, 54-517A, 77 Mass. Ave. M.I.T., Cambridge, MA 02139, USA.
E-mail address: qinc@mit.edu (Q. Cao).

0031-9201/$ – see front matter © 2010 Elsevier B.V. All rights reserved.
doi:10.1016/j.pepi.2010.02.006

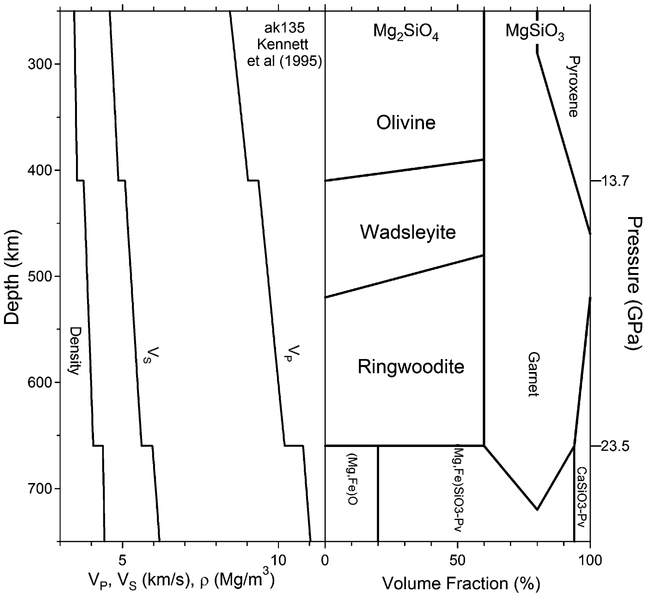

Fig. 1. (Left) *P*- and *S*-wavespeed (and mass density) as function of depth in Earth's mantle between 200 and 800 km depth according to reference Earth model *ak135* (Kennett et al., 1995). (Right) Volume fraction of the main mantle constituents in this depth range according to the pyrolite model of mantle composition. About 60% of the volume fraction concerns the olivine system, with phase transitions from olivine to wadsleyite near 13.7 GPa (associated with the first-order discontinuity in elastic parameters at 410 km in the *ak135* mode), wadsleyite to ringwoodite near 16–18 GPa (that is, around 510 km, but notice that there is no corresponding wavespeed or density contrast in the global reference model), and ringwoodite to perovskite and ferropericlase near 23.5 GPa (associated with a change in elastic parameters around 660 km depth). The remaining 40% of the volume fraction mainly concerns silicates in the pyroxene and garnet system.

Flanagan and Shearer, 1998a,b; Helffrich, 2000; Shearer, 2000; Gu and Dziewonski, 2002). Furthermore, the inferred global depth variations in '410' are generally smaller than in '660' (Shearer and Masters, 1992; Flanagan and Shearer, 1998a,b; Gu et al., 2003; Gu and Dziewonski, 2002), even though its Clapeyron slope is steeper.

Such inconsistencies suggest that published topography estimates or laboratory measurements are inaccurate or that more complex compositions and mineralogy must be considered. Laboratory experiments show that the depth to, the magnitude and transition profile of radial changes across discontinuities depend not only on temperature and pressure but also on, for instance, major element composition and partitioning, and the presence of water or (silicate) melt (e.g., Weidner et al., 2005; Li and Liebermann, 2007). Seismological evidence for such complexity has begun to emerge (Deuss et al., 2006), and manifestation of these effects on different length scales may degrade global-scale correlation between the depth variations of the discontinuities.

To enable better estimation of *in situ* mantle temperature, mineralogy, and composition from seismic data we must improve our capability to detect, image, and characterize seismic discontinuities. Receiver functions and near-source reflections have been used for regional-scale imaging of mantle discontinuities beneath dense receiver arrays or near (deep) seismic sources (Collier and Helffrich, 1997; Castle and Creager, 2000; Rondenay et al., 2005; Zheng et al., 2007; to name a few). Here we develop a method that can improve detection and imaging of transition zone over large geographical regions (including those far away from sources and receivers) with broadband *SS* data (Fig. 2).

Since the pioneering studies by Shearer (1991), most attempts to determine lateral variations in the depth to the main upper mantle discontinuities with *SS* and *PP* and their precursors have employed some form of common-midpoint (CMP) stacking (e.g., Shearer and Masters, 1992; Shearer, 1993; Gossler and Kind, 1996; Gu et al., 1998; Flanagan and Shearer, 1998a,b; Gu and Dziewonski, 2002; Chambers et al., 2005a,b; Schmerr and Garnero, 2006; Houser et al., 2008; Lawrence and Shearer, 2008), with the midpoint corresponding to the bounce point of the *SS* or *PP* waves. This method – see Deuss (2009) and Rost and Thomas (2009) for recent reviews – involves the stacking of (move-out corrected) waveforms over spatial bins followed by a time-to-depth conversion using a standard 1D reference Earth model (and corrections for 3D heterogeneity inferred from tomography). The size of the geographical bins used is often chosen to correspond loosely to the scale of the Fresnel zone of the associated *SS* or *PP* data, and stacking over bins with a radius of 10° is common (Deuss, 2009), but the complex shape of the Fresnel zone (e.g., Neele et al., 1997; Chaljub and Tarantola, 1997; Zhao and Chevrot, 2003; Dahlen, 2005) can be accounted for to increase spatial resolution (Lawrence and Shearer, 2008). Fundamentally, however, stacking over geographical regions implies substantial spatial averaging and thus the full resolving power of migration has been lost.

In contrast to stacking over bins followed by migration, methods based on inverse scattering directly localize and characterize point scatterers, and the spatial alignment of these scatterers then outlines a scatter interface or "reflector". This localization is based on the intersection of isochron surfaces and can be done with a spatial resolution much better than the Fresnel zones of the associated waves. With synthetic data, Shearer et al. (1999) demonstrated the potential of least-squares Kirchoff migration (inversion) of *SS*

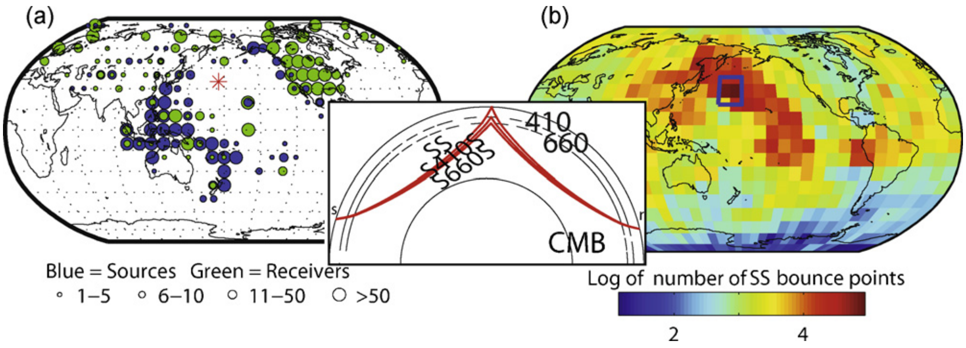

Fig. 2. (a) Distribution of sources and receivers of the data used in this study. The location of the image gather of Fig. 9 is shown by the red asterisk. The size of the blue (green) circle scales with the number of sources (receivers). (b) Global distribution of *SS* bounce points for data with a source–receiver distance of 90–170°, magnitude above 5.5 and focal depth below 75 km. Sampling density is indicated from red (densest) to blue (least dense). The solid blue rectangle outlines the 20° × 20° area in which data is collected. The ray paths of *SS* and its precursors are shown in the middle of the figure. The image point locations, which are near the midpoint of *SS* raypath, are far away from both the sources and receivers. (For interpretation of the references to color in this figure legend, the reader is referred to the web version of the article.)

precursors for high-resolution imaging of upper mantle discontinuities. Application to the then available data yielded noisy images, however, with few, if any, laterally coherent structures. To suppress effects of 'noise' (in the presence of uneven data coverage) Shearer et al. (1999) 'damped' the inversion, but the implied spatial smoothing rendered images at a spatial resolution similar to that obtained from the above-mentioned time migration followed by time-to-depth conversion.

Given the spectacular increase in data quality and quantity – nicely illustrated in Fig. 2 of Houser et al. (2008) – it is likely that application of the Kirchoff migration introduced by Shearer and co-workers a decade ago would now give more satisfactory results. But it is also possible to improve the inverse scattering method itself. We present here a generalized Radon transform (GRT), which has better noise-suppression capabilities than Kirchoff migration (because of the different use of data redundancy) and it accounts differently for complex wave phenomena such as caustics. The GRT was first used for seismic imaging in the 1980s (Beylkin, 1985; Miller et al., 1987), see reviews by Rondenay et al. (2005) and Gu and Sacchi (2009), but in recent years it has been used for large-scale imaging of deep mantle structure with *ScS* (Chambers and Woodhouse, 2006; Wang et al., 2006; Ma et al., 2007; Van der Hilst et al., 2007) or *SKKS* (Wang et al., 2008).

The main objective of this paper is to present a 3D GRT of the *SS* wavefield (including precursors) and to demonstrate the feasibility and promise of using this GRT for high-resolution transition zone imaging even far away from sources and receivers. We focus this feasibility study on the transition zone beneath the northern part of the Pacific Ocean (Fig. 2) because the density of *SS* bounce points is high and because it is far away from known subduction (along NW Pacific island arcs) and presumed upwelling (beneath Hawaii) so that not much structural complexity is expected. In the sections below, we present the method, describe the selection and processing of data, illustrate the performance of the 3D GRT on synthetic data, and – as a proof of concept – present (for different frequencies) a 2D, a 20°-long seismic section of the transition zone.

2. Methodology

2.1. Concept of inverse scattering

Inverse scattering uses signal from a large number of seismic data to localize elasticity contrasts in the sub-surface by determining how much scattering (reflection) at a specific point $y = (x, y, z)$ contributes to observed signal in recorded seismograms. Data in a narrow time window of a record associated with a fixed source–receiver pair can be due to scattering anywhere along a surface of constant travel time from source to scatter point to receiver. This isochron, in its finite-frequency form, is, in fact, the sensitivity kernel for inverse scattering. [We note that in analogy of ray paths versus finite-frequency kernels for transmission and reflection tomography (e.g., Dahlen et al., 2000; De Hoop and Van der Hilst, 2005; Tromp et al., 2005; De Hoop et al., 2006), in the context of ray theory the isochron would have an infinitesimally narrow width, but in finite-frequency theory the isochron would have multi-scale properties.] The distribution of sensitivity along each isochron is generally non-uniform and is determined by the intersection of the isochron with the Fresnel volume of the scattered phases. The total data sensitivity to structure at a certain sub-surface location is then the cumulative contribution from all isochrons through that point. While fully accounting for Fresnel zones, this allows the resolution of structure at the Rayleigh diffraction limit, at scales smaller than the Fresnel zones of the associated phases (Spetzler and Snieder, 2004), provided that data from a sufficiently broad distance and azimuth range is available in order to suppress imaging artifacts (Stolk and De Hoop, 2002).

2.2. The generalized Radon transform (GRT)

Because the development of the GRT used in our study follows closely the formulation for lowermost mantle imaging with *ScS* and *SKKS* reflections (Wang et al., 2006, 2008) we only mention the most relevant aspects. In essence, the GRT estimates the locations of local contrasts in elasticity (scatter points) in Earth's interior from their contribution to the scattered wave field. With the single scattering (Born) approximation, these contrasts δc are considered local perturbations in density and elasticity relative to a smooth background c_0. For our application, the smooth background model is derived from the *ak135* reference Earth model (Kennett et al., 1995) by replacing the first-order transition zone discontinuities by gradual transitions in wavespeed (Fig. 5), and the interfaces that we aim to image are thus represented as perturbations relative to this smooth background.

The data used by GRT, that is the wavefield δu due to scattering at δc, is modeled as

$$\delta u = F\delta c, \tag{1}$$

with F a single scattering operator. To estimate δc from the data one can set up the normal equations,

$$F^* F\delta c = F^* \delta u, \tag{2}$$

where F^*, the adjoint of F, is the imaging operator. Using ray theory, F^* yields a GRT while composition with the "inverse" of the normal operator F^*F adapts the weighting of the GRT to form an inverse scattering transform:

$$\delta c = (F^* F)^{-1} F^* \delta u. \tag{3}$$

The geometry of the problem is illustrated in Fig. 3. For each source–receiver pair, most of the energy in the recorded wavefield arrives at a time corresponding to a minimum or maximum two-way (reflection) travel time (T) path, which is commonly referred to as the specular reflection. For mini-max travel time phases (such as SS, $S_{410}S$, and $S_{660}S$), propagation along non-specular propagation paths can produce weak arrivals before or after the main phases. Conversely, for a given source–receiver geometry, arrivals in narrow time interval around a time t can be produced by scatterering anywhere along an isochron defined by $T(x^s, x^r, y) = t$, with x^s and x^r the position of the source and receiver, respectively (Fig. 3a). In essence, the GRT uses data δu in narrow time windows around t to characterize the strength of scattering at y: for a given sub-surface point y the time t (and the data window used) depends on the source–receiver combination, and for a given (x^s, x^r) record t depends on the position of y (Fig. 3b).

The total data sensitivity at a particular point y is the accumulation of sensitivities from isochrons $t = T(x^s, x^r, y)$ for all source–receiver pairs, weighted by the data in a narrow window around the corresponding time. To describe this process we introduce the migration dip ν^m, which is the normal to the isochron at the sub-surface point y for which the contribution to observed data is to be computed (Fig. 3c). For a (broken) ray path connecting a source at x^s with a receiver at x^r via y, we define p^s as the slowness vector (at y) for the ray from x^s to y, and p^r is defined similarly for the ray from x^r to y. These slownesses define the migration dip $\nu^m = p^m/|p^m|$, with $p^m = p^s + p^r$, and the scattering angle θ and azimuth ψ (Fig. 4c). Conversely, ν^m and (θ, ψ) determine p^r, p^s at y, and hence the corresponding x^s, x^r and $t = T(x^s, x^r, y)$. We can thus view the data δu associated with image point y as a function of ν^m, θ, and ψ – see Wang et al. (2006).

For each sub-surface point y an image gather $I(y;\ \theta,\ \psi)$ is obtained by integrating over all isochrons (with migration dip ν^m) that pass through y, with each contribution weighted with the cor-

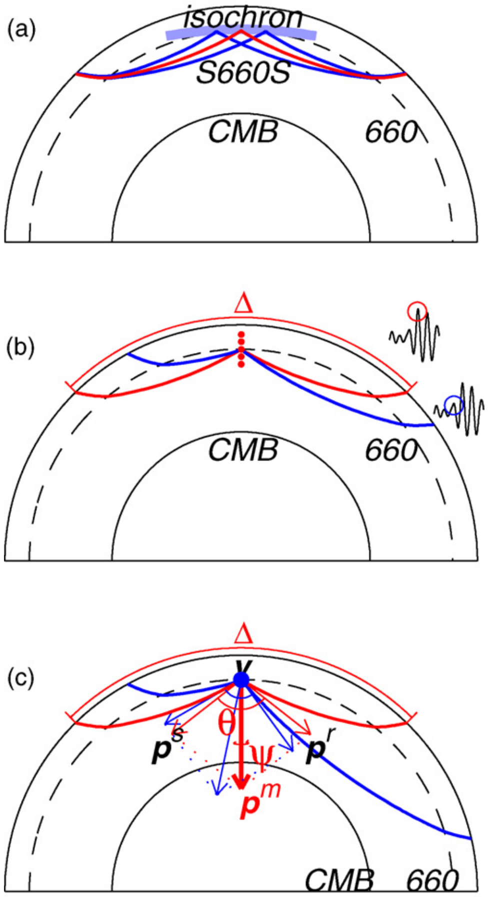

Fig. 3. Geometry of the GRT. (a) Illustration of an isochron, from which all reflections arrive at the same time. (b) Specular (red) and non-specular (blue) ray paths for a single scattering point. Because *SS* is a mini-max time path, waves that travel non-specular paths may arrive before or after the specular ray. Ray theory uses only specular data (red circle on waveform at right); the full GRT utilizes non-specular energy as well (blue circle). (c) GRT geometry for both specular (red) and non-specular (blue) paths. Unmarked arrows represent slowness vectors p^r and p^s at image point y. Scattering angle θ denotes the angle between the slowness of each leg of the ray path, evaluated at y. The migration dip ν^m describes the isochron normal at y. The scattering azimuth ψ describes the angle between North and the projection of ν^m onto the surface. (For interpretation of the references to color in this figure legend, the reader is referred to the web version of the article.)

responding data sample δu and weights W and w that control the sensitivity along the isochrons surfaces:

$$I(y;\theta,\psi)=\int_{E_{\nu m}}\frac{\delta u(y;\nu^m,(\theta,\psi))|p^m|^3}{W(y;\nu^m,(\theta\,\psi))^2|w(y;\nu^m,(\theta,\psi))|}d\nu^m. \tag{4}$$

Here, w accounts for ray geometry and places more weight on the specular reflection; W can be used to account for radiation patterns but is not implemented here. A structural image at y can be obtained through statistical inference (Ma et al., 2007) or, as is done here, through integration over θ and ψ:

$$I(y)=\int\int I(y;\theta,\psi)d\theta d\psi \tag{5}$$

For constant (x, y), (5) yields a radial reflectivity profile at a particular geographic location, and lateral juxtaposition of such 1D profiles would give a 2D seismic section.

We note that for underside reflections the range of scattering angles that can be used depends on the depth to the image point y (or interface depth d): the scattering angle generally θ increases (and the radial resolution decreases) with increasing depth of the imaging points and decreasing epicentral (source–receiver) distance (Fig. 2). Conversely, shallower signal is expected to appear in gathers for smaller θ and structure at greater depth appears at larger θ. This phenomenon, which we refer to as “spatial resolution drift”, requires binning in θ.

3. Data

For this pilot study we consider the northern Pacific, where the density of *SS* bounce points is high owing to the abundance of sources and receivers along the plate margins and continents surrounding the Pacific basin (Fig. 2). For *SS* waves with bounce points in a 20° × 20° area from 25° to 45°N and 160° to 180°E we retrieve broadband waveforms from the Data Management Center (DMC) of the Incorporated Research Institutions for Seismology (IRIS). We use hypocenter parameters from the EHB catalog due to Engdahl et al. (1998).

The data selection criteria are rather similar to those used in other *SS* studies (Deuss, 2009). For data at epicentral distances from 90° to 170° we extract time windows containing *SS* proper and precursors due to scattering in the transition zone. We note – and demonstrate – that interference with phases other than *SS* precursors does not visibly degrade the GRT images. The minimum source magnitude is $m_b = 5.5$ and focal depths are less than 75 km (to reduce contamination by depth phases). Fig. 4 displays a (transverse component) record section of the data used here, aligned on *SS*, along with predicted travel times according to *ak135*. This record section reveals $S_{410}S$ and $S_{660}S$ phases at distances less than 130°, with $S_{660}S$ appearing stronger than $S_{410}S$, and arrivals between $S_{410}S$ and $S_{660}S$.

For the data that pass the initial selection criteria we add event parameters from the EHB catalog to the file headers, check (and, if needed, correct) polarization, deconvolve the instrument response, rotate the data to radial and transverse direction, and then use a 4-pole Butterworth filter to bandpass the data between 20 and 50 s, 10 and 50 s, 5 and 50 s, and 2 and 50 s, respectively, in order to study the frequency dependence of the images. Subsequently, the traces are Hilbert transformed and normalized with respect to *SS*. For the shorter period data (that is, for the $T = 2$–50 s and $T = 5$–50 s bands considered below) we apply a signal-to-noise criterion (with the signal-to-noise ratio defined as the ratio of peak amplitude of *SS* proper signal to the maximum amplitude of the whole window containing *SS* proper and precursors) and discard data with signal-to-noise ratio smaller than 1/5.

All available data can be used for the calculation of total data sensitivity to structure at a given point y, but to reduce the computational burden and interference with other phases we restrict the computation to records associated with rays with a specular reflection within a certain distance (here 6°) from y. We stress that waveforms are not stacked over these bins and recall that for each image point y a different time window is extracted from a seismogram, so that the total data sensitivity to structure at y is independent from that at adjacent sub-surface image points. Upon imaging, travel times are determined through table interpolation with time corrections for 3D structure from tomography (Grand, 2002).

4. Tests with synthetic data

We tested the performance of the generalized Radon transform of *SS* precursor with inversions of synthetic data. In all tests, we compute the synthetic wavefields using the actual earthquake-station distribution so that influence on the image of uneven data coverage, including the effects of a realistic focal depth distribution, is the same as for the inversion of the recorded wavefields.

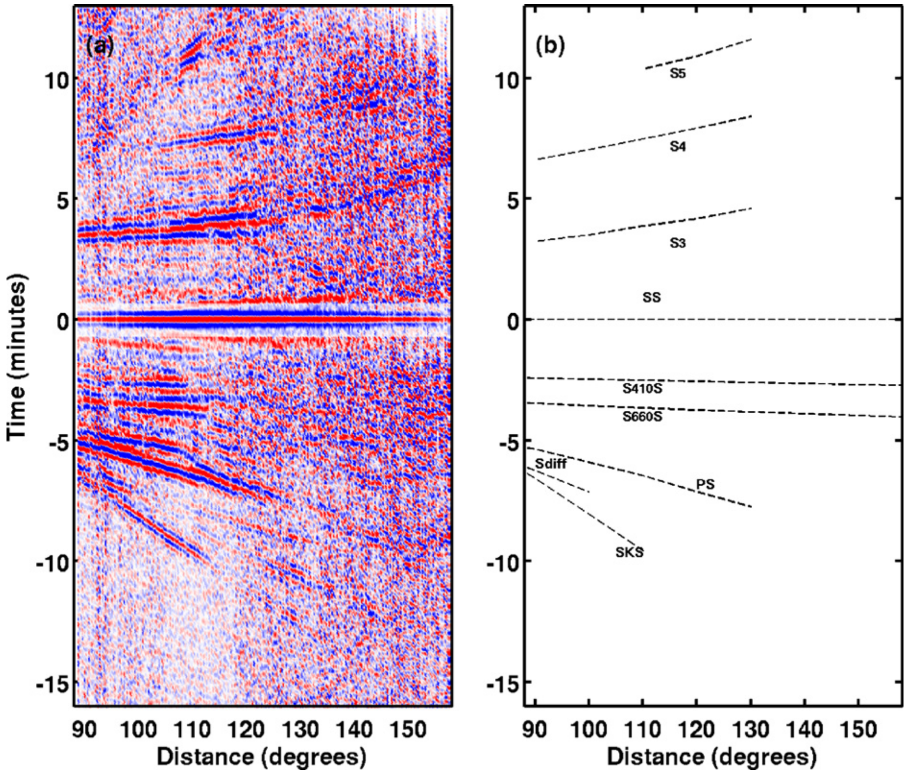

Fig. 4. (a) Record section of data with reflection points in the study area shown in Fig. 2. The stack is relative to the *SS* phase. (b) Corresponding travel time curves (according to *ak135*). We use data beyond 90° (to avoid polarity reversal of $S_{660}S$) up to 170° (to avoid non-specular rays interacting with the outercore). The data has been bandpass filtered between 20 and 80 s. For this geographic bin (Fig. 2) there are relatively few data for epicenter distance larger than 115°; as a result the expression of the precursors is weaker than in global stacks due to, for instance Shearer and Masters (1992).

In a first series of tests we use WKBJ (Chapman, 1978) synthetics to show that the generalized Radon transform of *SS* precursor data can detect and locate elasticity contrasts in the presence of noise, *P*-to-*S* phase conversions, depth phases, and multiple reflections. For this purpose synthetics for the *SS* wavefield (including $S_{410}S$ and $S_{660}S$) are computed for *ak135*; we use the same source function for all waveforms and the data are filtered using a pass-band of 20–80 s. These synthetics represent the total wavefield $u = u_0 + \delta u$. Upon inversion, we seek to infer from δu the elasticity perturbations δc relative to a smooth reference model c_0 (associated with u_0) which, as mentioned above, is obtained from *ak135* by smoothing the step-wise velocity increases over a broad depth range.

With another type of test we demonstrate that the GRT can resolve structure at scales smaller than the Fresnel zones of the associated scattered waves. For this purpose we follow Shearer et al. (1999) and invert data generated (using the Born approximation) for interfaces with topography and gaps.

4.1. Image gathers

We first use WKBJ synthetics to see how interfaces at 410 and 660 km appear in the image gathers. Synthetics are computed for *ak135* (that is, with step increases in shear wavespeed at 410 and 660 km depth, but no contrast near 520 km). The GRT seeks to locate perturbations with respect to the smooth back ground. This test would be considered successful if the GRT yields contrasts near 410 and 660 km (and nowhere else).

Using (4) we form image gathers $I(y;\,\theta,\,\psi)$ for image points y at 5 km depth intervals along 1D (radial) profiles from Earth's surface to 1000 km depth—note the amplification (by factor of 4) for depths larger than 100 km. Integration over scattering azimuth ψ and combining the results in bins of scattering angle θ yields a series of common image point gathers spanning the whole range of θ but with varying sensitivity to structure at different depths (Fig. 5). The latter is a manifestation of "spatial resolution drift" (see note at the end of Section 2.2): shallow interfaces appear

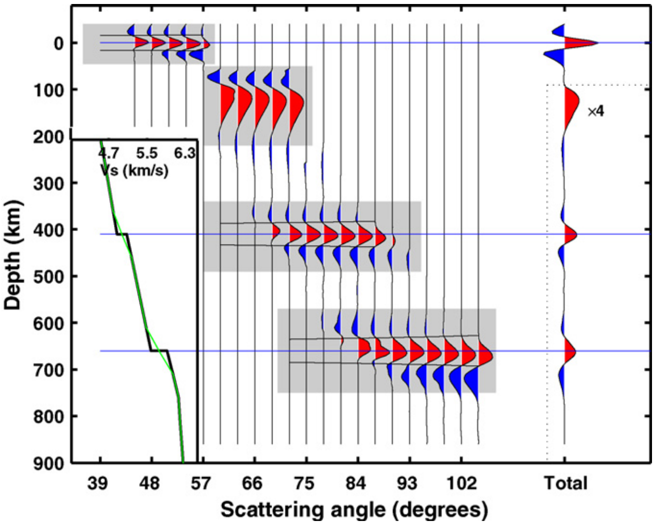

Fig. 5. GRT applied to synthetic (WKBJ) data with actual source–receiver distribution and focal depth (periods 20–80 s). Traces are normalized so that signal strength cannot be compared across scattering angle. Side lobes of the surface signal are similar in amplitude to the 410 and 660 signals. The common image gather (right) is amplified (4×) below the dash line. Inset at lower left: the thick dark line represents the original *ak135* velocity model (with first-order discontinuities at 410 and 660 km depth), from which the synthetic wavefield is computed; the thin green line represents the smooth model which we used as the background model c_0 for the GRT. (NB because they are replaced by broad gradients, the results do not depend on discontinuity depth and strength of the original *ak135* model.) The structure around 150 km depth is a blow up of one of the side lobes of the surface reflection *SS*.

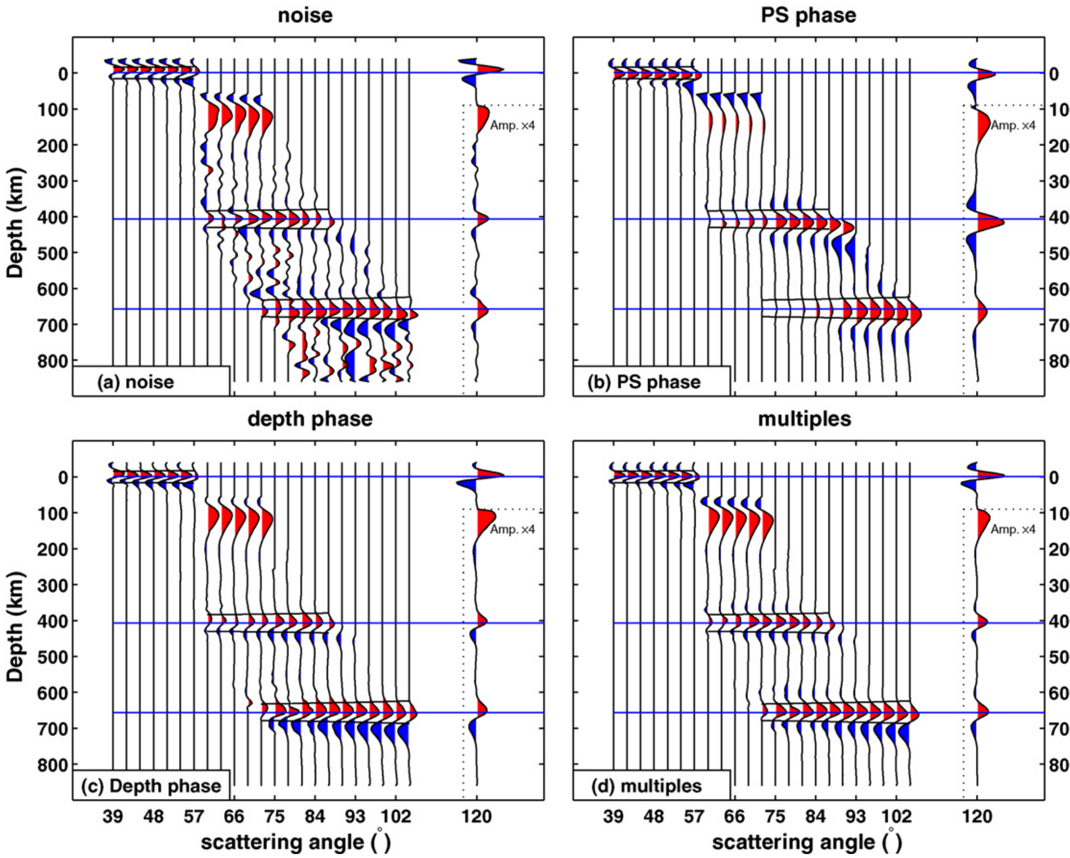

Fig. 6. Effects on the GRT images of white stationary noise (a), the presence of *P*-to-*S* converted phases (b), presence of depth phases (c), and multiples reverberations between transition zone discontinuities (d). Adding these effects to the synthetics of the *SS*, $S_{410}S$, and $S_{660}S$ has little effect on the GRT image gathers.

for scatter angles $39° < \theta < 60°$, the '410' discontinuity appears at $60° < \theta < 90°$, and scatter angles between 70° and 105° reveal the '660'. Integration over all θ reveals structure along the entire vertical profile (Fig. 5, trace on the right). This GRT image shows peaks at the correct depths of 0, 410 and 660 km, and we note the absence of reflectivity contrast at depths other than 410 and 660 km. The amplitude of the peaks at 410 and 660 are comparable, and the widths are about 50 km (slightly more for 660 than the 410 because of the scatter angles generally being larger) which is consistent with the frequencies used. We have verified that peak location and width are insensitive to the (smooth) background velocity model.

4.2. *Effects of noise, phase conversions, depth phases, or multiple scattering*

With similar experiments we examined the effects on the image gathers of noise or the presence of *P*-to-*S* conversions, depth phases, or multiple reverberations. We first ran the GRT on WKBJ synthetics that include white stationary noise, with signal-to-noise ratios between 1/20 and 1/100 for both $S_{410}S$ and $S_{660}S$ and 1/5 for *SS* proper. Even though the precursors cannot be identified in the raw data, the GRT image gathers reveal the contrasts at 410 and 660 km well above the noise level (Fig. 6a). Fig. 4 suggests that *PS* waves can arrive close to the *SS* precursors. Likewise, depth phases from deep earthquakes and multiple reflections of and reverberations between transition zone discontinuities can interfere with the *SS* precursors (e.g., Schmerr and Garnero, 2006). Applying the GRT to synthetic wavefields containing such signals demonstrates that such interfering waves do not, in general, contaminate the images of the '410' and '660' (Fig. 6b–d). Converted phases such as *PS* and multiple reverberations can form prominent arrivals but the difference in slowness is sufficient to suppress them upon transformation (Fig. 6b and d). Depth phases could contaminate the image gathers if events occurred in a small depth range, but for the (realistic) depth distributions considered here the depth phases do not produce spurious 'events' in the image gathers. However, they can produce small phase shifts (pulse distortions) (Fig. 6c). From these and other tests we conclude that seismic phases other than *SS* and its precursors do not produce major artifacts. [Caveat: since WKBJ synthetics only contain user-specified dynamic wave groups we cannot rule out the possibility that there are interfering phases that could produce imaging artifacts—more comprehensive tests require full wave synthetics, for instance from mode summation or reflectivity method.]

4.3. *Lateral resolution*

To test lateral resolution, and demonstrate that inverse scattering can resolve structure at length scales smaller than the Fresnel zone of the scattered waves, we use the GRT in a synthetic example similar to the one used in Shearer et al. (1999). The model (lower right corner of Fig. 7) consists of a 220-km reflector east of 196°E, a flat 410-km discontinuity with a 4° wide gap near 192°E, and an undulating 660-km discontinuity with a strong topographic gradient around 195°E and a smooth change in depth east of 210°E. The 2D interfaces vary with longitude and are invariant in latitude. Using the Born approximation, and with fixed source—time function, synthetic data is generated with the real source and receiver distribution. The effective bandwidth of the

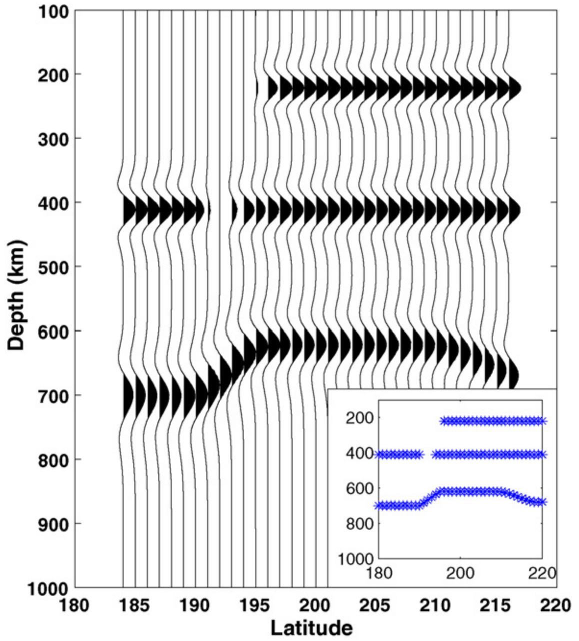

Fig. 7. Result of inversion with synthetic data to test lateral resolution. The model for which synthetic data is computed (using Born approximation) is plotted in the lower right corner. The input model, which is similar to that used by Shearer et al. (1999), consists of a local 220-km reflector, a discontinuous yet flat 410-km discontinuity, and an undulating 660-km discontinuity with both a strong topographic gradient and a smooth change. The GRT result is shown in the main panel. Despite some smearing effects, the major features are well resolved.

scattered data is ∼20 s, and the lateral extent of the associated Fresnel zone would be of the order of 1000 km. The result of inverse scattering with our GRT is shown in the main panel of Fig. 7. Despite some smearing effects, the major features (termination of the '220', the gap in the '410', and the topography of the '660') are well resolved.

5. Preliminary images of the transition zone beneath the Northwest Pacific

The ∼50,000 records displayed in Fig. 4 are used for 3D GRT imaging of the transition zone beneath the Northwest Pacific (Fig. 2a). First, we examine the GRT image at (35°N, 175°E). Subsequently, 21 such radial reflectivity profiles are juxtaposed to form a 2D, north–south seismic section from (25°N, 175°E) to (45°N, 175°E) (Fig. 8). We recall that for the inversion of real data we correct the travel times for 3D mantle heterogeneity using the tomographic model due to Grand (2002). The effect on the images is small, and the results do not depend strongly on the choice of model, but we note that subtle pulse complexities may be introduced (or removed) when using (different) 3D mantle models.

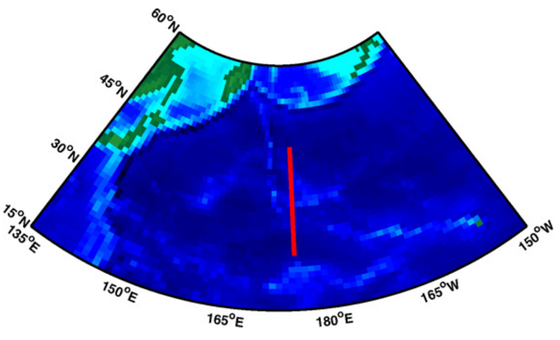

Fig. 8. The location of the line of section for which images are shown in Figs. 10 and 11.

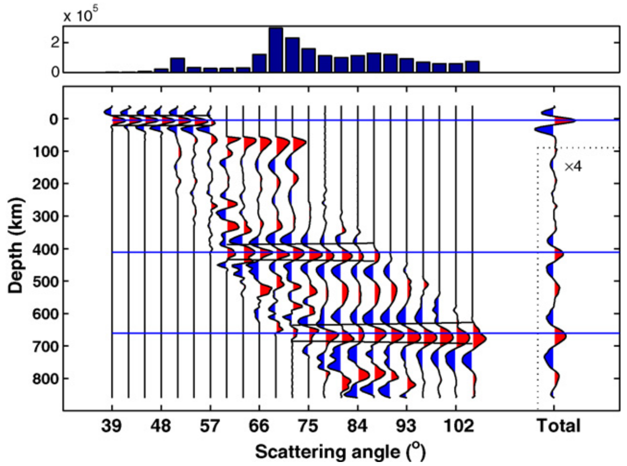

Fig. 9. Construction of GRT (reflectivity) image (single trace on the right) from 'common image point gathers' for broadband *SS* data (10–50 s) for a range of opening angles (traces on the left of this panel). The panel above shows the number of data samples used for the computation of the traces at specific θ.

Fig. 9 displays the angle gather and resulting GRT image for a location with coordinates (35°N, 175°E). The radial images as a function of scattering angle θ (traces on the left) are produced by integration (for fixed θ) over scattering azimuth ψ. The number of data samples used to calculate the traces at specific θ, plotted above the angle gather, is fairly constant over the range of scatter angle used. For narrow ranges of θ the angle gathers reveal structure in a limited depth range, as discussed above, but integration over θ yields a GRT image that reveals multiple peaks, including contrasts near 410, 520, and 660 km depth (Fig. 9, trace on the right). There is also signal above 410 km and below 660 km depth, but in isolated profiles the robustness and significance of such signals are not easily evaluated. Next, we create angle gathers and GRT reflectivity profiles for points 1° apart along the north–south line depicted in Fig. 8, and lateral juxtaposition of them creates a 2D seismic section from the surface to 1000 km in depth (Figs. 10 and 11). For display purposes, and to highlight deeper structures, the near-surface signal has been muted in the images.

In Fig. 10a we display the radial GRT profiles for data filtered between 20 and 50 s superimposed on the tomographically inferred lateral variations in shear wavespeed (Grand, 2002) that are used to construct the image. The other panels of Fig. 10 display the GRT images computed from data with a decreasing short-period band lower limit (10, 5, and 2 s, respectively). In Fig. 11 we display for the same four bandwidths the seismic sections after lateral interpolation between the radial profiles. At all frequencies, and along the entire 2D section, the data yield large-amplitude, laterally continuous and uniform signals near 415 and 665 km depth. A weaker, but laterally continuous signal appears near 520 km, but its appearance changes considerably with frequency. Hereinafter we refer to these reflectors as the '410', '660', and '520'. The images also reveal scatter zones in the upper mantle (that is, less than 410 km depth) and in the shallow part of the lower mantle between 800 and 1000 km depth, but their strength and depth vary considerably.

Fig. 12 shows *SS* stacks at three positions along the section line shown in Fig. 7 (personal communication, A. Deuss, 2008). On the right-hand-side we plot the average reflectivity along the entire section presented–this trace represents the stack of all 21 GRT images (reflectivity profiles) shown in Fig. 10b. The excellent agreement suggests that on a lateral scale of the order of 1000 km, and for relatively low frequencies, the GRT images are in excellent agreement with those produced by common midpoint stacking.

For all frequency bands considered, the '410' and '660' discontinuities are prominent features in the seismic sections. In the low

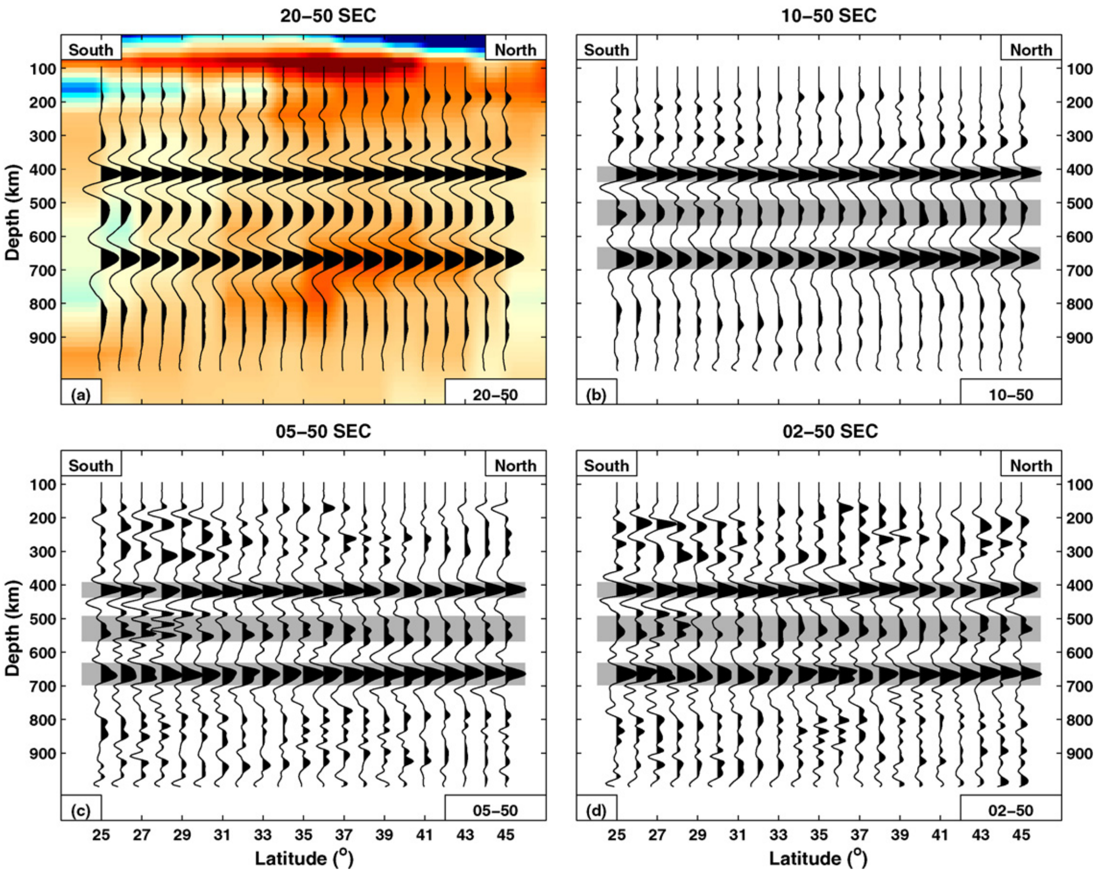

Fig. 10. Seismic sections of the mantle transition zone in the northern Pacific (see Fig. 8 for section location) for different frequencies of the data used. The 2D section is constructed by lateral juxtaposition of radial reflectivity profiles calculated using Eq. (5) and the (raw) data associated with the record section in Fig. 4, filtered between (a) 20 and 50 s, (b) 10 and 50 s, (c) 5 and 50 s, and (d) 2 and 50 s. The surface signal is excluded to highlight the weaker structure. Each trace is normalized by its maximum. The '410' and '660' are continuous along the entire length of the section and appear without much change in all the four frequency bandwidths. The '520' is prominent at low frequencies (periods $T = 20$–50 s, panel a) but becomes increasingly more incoherent when shorter period data are included. Background colors in panel (a) depict lateral variations in shear wave speed according to the tomographic model of Grand (2002). In panels (b)–(d) the grey bars indicate the location and width of the pulses associated with the 410, 520 and 660 in the 20–50 s period range (panel a). (For interpretation of the references to color in this figure legend, the reader is referred to the web version of the article.)

frequency band, 20–50 s (Figs. 10a and 11a), the appearance of the '410' and '660' along the section is remarkably stable. The '660' appears somewhat wider than the '410' but part of this reflects the above-mentioned decrease in radial resolution due to the fact that the deeper structures are constrained by larger scattering angles opening angles—indeed, this effect was also apparent in the synthetic tests (e.g., Fig. 5). At these frequencies the images reveal no significant topography on either the '410' or the '660'. With increasing frequency band the '410' and '660' remain stable but slight lateral variation in depth becomes apparent and the pulse shapes begin to reveal subtle complexity. For example, the pulse width and amplitude vary slightly along the line of section, and at some latitudes the pulses that delineate the '660' become more asymmetric (locally the '660' may even appear split). However, such subtle variations are probably within the uncertainty caused by 3D mantle heterogeneity and should interpreted considerable restraint. We observe that with increasing frequencies, the amplitude of the '410' decreases slightly compared to that of the '660'.

The '520' appears prominently in this region, especially at the lowest frequencies considered here. At periods between 20 and 50 s (Figs. 10a and 11a) it forms a laterally continuous scatter zone that is substantially weaker and broader than both the '410' and the '660'. For periods longer than 10 s the '520' shows prominently both in our GRT images and in the common-midpoint stacks for the same region (Fig. 12). When progressively higher frequencies are admitted, the structure of the reflectivity zone becomes increasingly complex and incoherent. At periods less than 10 s splitting of the '520' is common (Fig. 10b–d). This change in character is readily visible in the seismic sections displayed in Fig. 11b and c. Around 39°N, for example, the data suggest the presence of multiple (weak) elasticity contrasts, and the different branches of the '520' form a complex pattern between 500 and 550 km depth (Fig. 11c and d). The absence of comparable complexity in the '410' and '660', and the fact that the change in pulse shape with frequency is larger than the effects we have seen from 3D mantle heterogeneity, suggests that the structural complexity and frequency dependence of the '520' is real and neither caused by local changes in data coverage or quality nor due to mantle structure that is not well represented by the tomographic model used. At low frequencies, the depth to the '520' varies smoothly along the profile and the topography is positively correlated with the '410'. The topography is larger in the 10–50 s band, and at short periods the '520' is too incoherent to give a meaningful estimate of topography.

In addition to the unequivocal interfaces near (on average) 415 and 665 km depth and a complex (frequency dependent) scatter zone around 520 km depth, the GRT images reveal significant structure between 200 and 300 km depth and between 800 and 1000 km depth. At the longest periods considered here (20–50 s) these signals could reasonably be dismissed as side lobes of the $S_{410}S$ and $S_{660}S$ (Figs. 10a and 11a), but increasing the bandwidth demonstrates that they are distinct, unambiguous, albeit weak and perhaps laterally discontinuous structures. We also stress that the

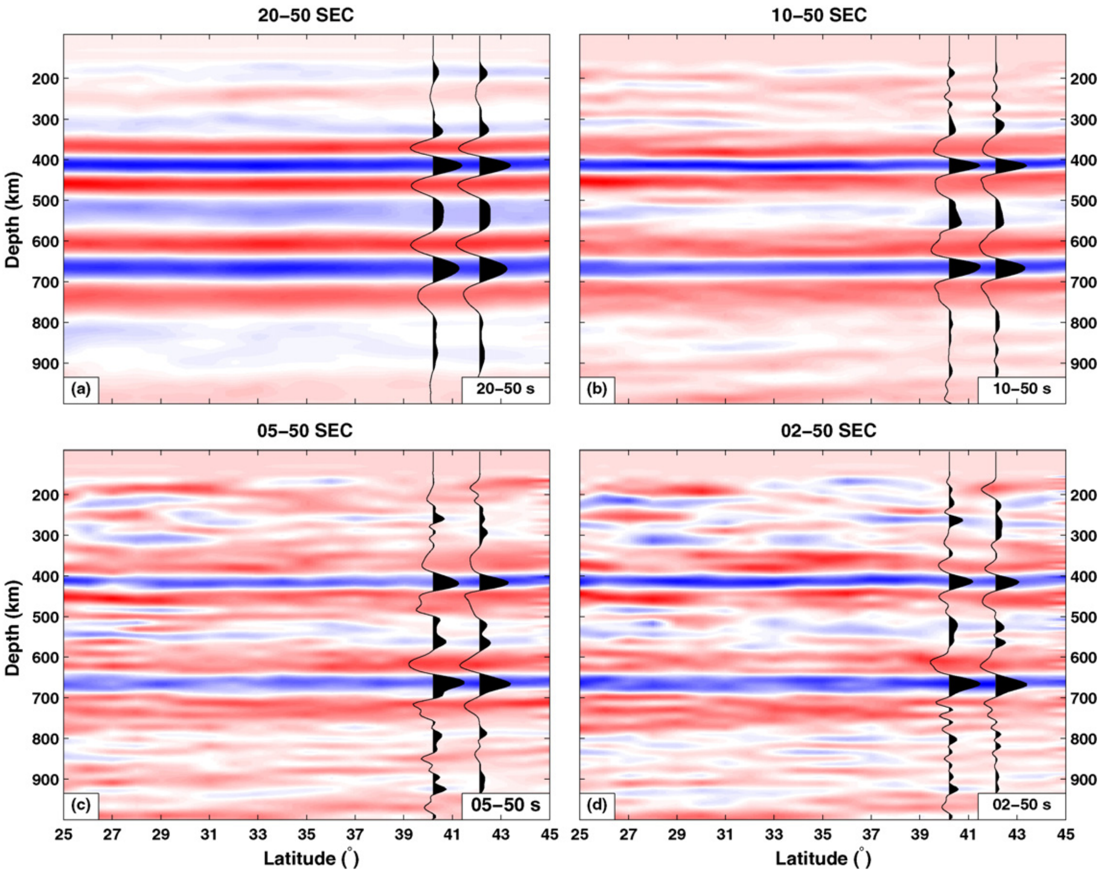

Fig. 11. Same seismic sections as in Fig. 10 but to enhance interfaces (for display purposes only) we interpolated between the traces. To facilitate comparison with the sections of Fig. 10, in each panel we also show (for the corresponding period band) the actual GRT image profile at two locations.

inversion of data computed for a model with only the ‘410’ and ‘660’ (Fig. 5) did not produce artifacts near 300, 520, or 800 km depth. Furthermore, in the 20–50 s and 10–50 s windows the topography of the event around ‘300’ does not correlate with that of the ‘410’, which also suggests that they are not related to one another in a simple way.

6. Discussion

6.1. *Transition zone imaging with the generalized Radon transform*

The results of the resolution tests with synthetic data, the robustness of inversions of recorded data, and the excellent agreement (evaluated at the appropriate scale) between the seismic sections presented and results of conventional common-midpoint stacking, demonstrate that transition zone imaging with the generalized Radon transform of the *SS* wavefield is feasible, at least in regions of dense data coverage such as the northern and northwestern part of the Pacific. A decade ago, Shearer et al. (1999) already demonstrated with synthetic data the promise of migration techniques for the imaging of transition zone discontinuities, but with the then available data coverage it did not appear possible to obtain results much better than common-midpoint stacking. To a large extent, the success of GRT imaging reported here can probably be attributed to access to vastly more data, but there are also subtle – but important – technical aspects of the methodology that help produce high-resolution images.

An important aspect of the GRT, as presented in this paper, is that it fully exploits the redundancy in the data and is not restricted to “common-offset” subsets of the data. The GRT constructs multiple images of a given image point for varying scattering angles and azimuths, and the final image for that location is then obtained by integrating (stacking) over these angles. This way of using data redundancy (that is, stacking over angle for a fixed image point versus stacking of waveforms over spatial bins) is a fundamental difference between the GRT used here and methods involving stacking over spatial bins, such as common-offset Kirchoff migration.

The approach described by Shearer et al. (1999) and the GRT presented here both solve an underdetermined (linearized) inverse

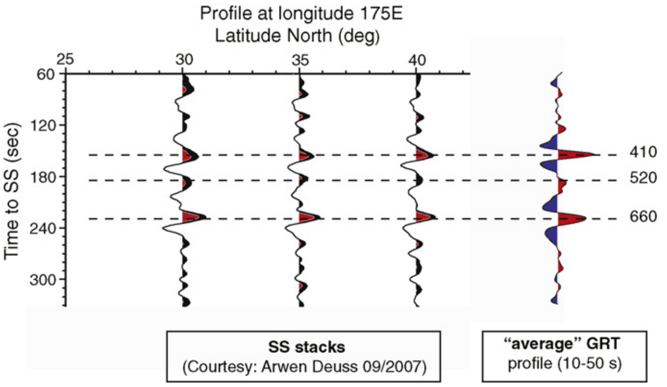

Fig. 12. Left: stacks of *SS* precursors for three locations along section shown in Fig. 8 (A. Deuss, pers. comm. 2007). Data (T = 10–50 s) are stacked over spherical caps with radius of 10° and for a reference distance of 130° (see also Deuss, 2009); no crust or 3D mantle correction is applied. Right: ‘stack’ of the 21 GRT images of Fig. 10B along the entire section; this stack of the GRT images implies averaging over ∼1000 km. The depth is scaled to time to facilitate the comparison.

problem. In the GRT the least-squares inversion is implicit through the inclusion of the approximate inverse of the normal operator F^*F, see Eq. (3). In the full implementation of the GRT, the normal operator controls the sensitivity along the isochrons by accounting for the radiation patterns (focal mechanisms and contrast source), geometrical spreading, and illumination. [We note that in our implementation we do not include all weights – see remark below (4).] Instead of Tikhonov regularization in the model space (which decreases spatial resolution), the GRT attributes sensitivity in accordance with the Fresnel zones of the relevant scattered phases by limiting the range of integration over migration dips, which is controlled by the available data. Applied to unevenly sampled data, the GRT accumulates the contributions from the corresponding sensitivity kernels weighted with available data samples. This localization of sensitivity, akin to the use of finite-frequency sensitivity kernels in transmission or reflection tomography, reduces the need for regularization (spatial averaging) and preserves lateral resolution where illumination is sufficient.

Adequate localization of sensitivity requires data from a broad distance and azimuth range (Stolk and De Hoop, 2002), and in regions with poor data coverage (in terms of the range of scattering angles and azimuths) application of the GRT as presented here may produce imaging artifacts. In such regions it may still be possible to constrain some aspects of sub-surface scatters if one can achieve even better localization than is possible with the traditional GRT. The optimal way to implement such partial reconstruction with the GRT, in multi-scale sense, makes use of wave packets and localization in phase space (De Hoop et al., 2009), and this is a topic of further research.

6.2. *Transition zone structure and mineralogy*

The region studied here is far away from the northwestern Pacific subduction zones and the presumed mantle upwelling beneath Hawaii. The 2D section crosses the Hawaii-Emperor seamount chain (around 30°N). Inverse scattering of *SS* data can in principle resolve topography at a lateral resolution of a few 100 km (Fig. 7), which is up to an order of magnitude smaller than obtained by traditional stacking of long-period *SS* data, but in this part of the tectonically stable Pacific the topography is (as expected) small and will, therefore, not be a topic of discussion here.

The data resolve scatter zones at several depths beneath the study region. The most pronounced and robust reflectors appear around 410 and 660 km depth, but the images also suggest elasticity contrasts around 300 km depth, between 500 and 560 km (especially at longer periods), and between 800 and 1000 km. The presence of interfaces near 410, 500–560, and 660 km depth is generally consistent with expectations from olivine mineralogy (Fig. 1). Scattering near 300 km and between 800 and 1000 km depth occurs outside the pressure/depth range associated with the transitions in the olivine system (which mark the transition zone *senso stricto*) and may be related to pyroxene and garnet transitions.

The depth to the '410' (averaged along the profile) is 415 km, and the '660' occurs around 665 km depth. At a wavespeed of 5 km/s the uncertainty in depth is about 5 km at the short-period range of the data used here, and inaccuracies in the background wavespeed of the order of 1% would add (at most) another 5 km to this uncertainty. With these estimates of uncertainty, the '410' and '660' are imaged approximately at their global average depths, and both the variation in depth along the line of section and the minor distortions of the pulses associated with the '410' and '660' km discontinuities are probably insignificant. The observation that with increasing frequencies the amplitude of the '410' decreases slightly compared to that of the '660' suggests that in this region the post-spinel (ringwoodite to perovskite and ferropericlase) transition (associated with the '660') is sharper than the olivine to wadsleyite transition (associated with the '410'). This is consistent with mineral physics studies that suggest that the olivine to wadsleyite transition occurs over a broader depth range (6–19 km) than the post-spinel transition (1–10 km) (Bina and Wood, 1987; Irifune and Isshiki, 1998; Ito and Takahashi, 1989; Katsura and Ito, 1989; Akaogi et al., 1989).

The images reveal substantial scattering from depths in between the '410' and '660' interfaces. This depth range is consistent with the wadsleyite to ringwoodite transition, which previous seismological studies have referred to as the '520' discontinuity (e.g., Shearer and Masters, 1992; Deuss and Woodhouse, 2001; Deuss, 2009). For data with periods larger than 10 s our images reveal a single broad event between 500 and 560 km depth (e.g., Fig. 11a). With increasing frequency the signal becomes weaker and increasingly less coherent, with (multiple) splitting observed in the GRT images at 5–50 s and 2–50 s (Figs. 10c, d and 11c, d). This complexity is not seen in the '410' and '660' and cannot (in a trivial way) be attributed to deterioration of data coverage at these periods. These observations suggest that the frequency dependence of the '520' is real.

Deuss and Woodhouse (2001) observe reflections near 500–515 km and 551–566 km in some regions of Pacific, near the Indonesian subduction zone, and beneath the North African shield. They attribute the splitting to the phase transitions in non-olivine (e.g., pyroxene, garnet) components. Saikia et al. (2008) proposed that the shallower discontinuity is due to the wadsleyite to ringwoodite transformation whereas the deeper one represents the formation of $CaSiO_3$ perovskite from garnet. In a fertile mantle – or in a mantle with a substantial component of recycled MORB crust, which contains more Ca than normal mantle – these two discontinuities would be separated. The regional variation of the character of the '520' has thus been invoked as evidence for large-scale chemical heterogeneity.

Alternatively, the predominance of the '520' at low frequencies and its gradual break-down with increasing frequencies of the data used may – to first order – be explained by the broad two-phase loop of the divariant transition from wadsleyite to ringwoodite (Shearer, 1996; Rigden et al., 1991; Frost, 2003). In peridotite mantle this transformation is found to take place over a pressure interval corresponding to ∼20 km at 1400 °C even when buffering by garnet is considered. Frost (2003) also showed that the phase-fraction profile is almost linear across the transformation, which would explain why its image is more pronounced for low frequency data. It is possible that the structure at short periods reflect transitions in the non-olivine components that become visible only when, with increasing data frequency, the image of the wadsleyite to ringwoodite transition weakens. We note, however, that this weak signal may not exceed the noise level (and its variability is within the uncertainty due to wavespeed variations that are not accounted for in the global tomography model that we use to make travel time corrections).

We have as yet no definitive explanation for the scattering that is visible near 300 km depth (Figs. 10a, b and 11a, b). One possible cause is the transition in pyroxene from an orthorhombic to a monoclinic structure (Woodland and Angel, 1997; Stixrude and Lithgow-Bertelloni, 2005). For a pyrolite mantle composition the effect of this transition on elasticity would be small but in material with higher concentrations of ortho-pyroxene, such as harzburgite, the change could be substantial. If this interpretation is correct, our results imply that even far away from zones of present-day subduction the upper mantle could contain significant fractions of harzburgite. Williams and Revenaugh (2005) proposed that a discontinuity at around 300 km might be generated by SiO_2-stishovite formation in eclogitic assemblages. This explanation would imply widespread occurrence of materials with mid-oceanic-ridge basalt chemistry. Finally, the '300' could signify the base of a zone of carbonatite melting in the asthenosphere (J.-P. Morgan, personal communication, 2009).

These are exciting possibilities, both with far reaching implications for our understanding of mantle flow and mixing. We are hesitant, however, to push the interpretation of the observation of scattering near 300 km depth beyond these speculations and defer further discussion to a later time when robust evidence is available for a larger geographical region. Yet we note that most of the above explanations require a chemistry that is distinct from a pyrolitic composition, which may suggest significant compositional heterogeneity in a region is (at present day) far away from active subduction systems.

7. Conclusions

We have developed a generalized Radon transform to construct the images of mantle transition zone with the broadband wavefield of *SS* and its precursors. The GRT is a technique for inverse scattering and it exploits the redundancy in the data in that for a range of scattering angle and azimuth it creates multiple images of a single point. Combined, these common image point gathers represent a GRT image (i.e., the radial reflectivity profile) which reveals the position of scatterers as a function of geographic location and depth beneath the surface. The main objective of this paper was to demonstrate the feasibility of high-resolution imaging of the transition zone beneath geographic regions (such as oceans) far away from sources and receivers. In future studies this new capability will be used for high-resolution studies of the transition zone beneath, for instance, Hawaii.

The GRT images of the transition zone beneath the north Pacific reveal a pronounced '410' and '660' for all frequencies considered. For periods $T > 10$ s our results are consistent with that of conventional *SS* stacking. With increasing frequency there is a slight increase in structural complexity and depth variation, and a strengthening of the '660' compared to the '410' (which may indicate that the former is sharper than the latter). The average depths to the '410' and '660' are 415 ± 5 and 665 ± 7 km, respectively, and the small ($\sim$10 km peak-to-peak) depth variation is insignificant given the depth resolution of the data. The '520' is pronounced in the low frequency band, and broader and weaker than either the '410' or '660', but there is an increase in the complexity of the '520' with increasing frequency, even when the '410' and '660' are not similarly affected. The frequency dependence of the '520' is consistent with the broad two-phase loop of the wadsleyite to ringwoodite transition, but structure that becomes visible at short periods may reflect transitions in non-olivine components.

In addition to the usual suspects (that is, the '410', '520', and '660'), the transition zone images also reveal substantial scattering from structures at around 300 km depth and between 800 and 1000 km depth. The prominence of the event near 300 km could indicate the presence of harzburgite or MORB material far away from sites of active subduction. These structures may be laterally intermittent, however, and larger scale imaging is needed to establish the geographical distribution and lateral continuity of these structures.

The vast and rapidly growing amount of high quality waveform data that is available through IRIS DMC has begun to allow large-scale exploration seismology of the deep mantle. Following our studies of the lowermost mantle with inverse scattering of the *ScS* and *SKKS* wavefields (Wang et al., 2006, 2008; Van der Hilst et al., 2007) we have demonstrated here the feasibility of transition zone imaging with the *SS* wavefield. This is opening exciting new possibilities for collaborative studies of Earth's deep interior in general and for detailed investigations of the upper mantle transition zone, in particular.

Acknowledgments

We thank Jason Phipps Morgan and Greg Hirth for stimulating discussions and excellent suggestions on various aspects of our work, and we are grateful to Arwen Deuss for computing the *SS* stacks shown in Fig. 12. We thank Rosalee Lamm (MSc, MIT) for her contribution to the early stages of this project. The revision of the original manuscript benefited greatly from insightful comments by Peter Shearer, an anonymous reviewer, and the Editor (George Helffrich). This research has been supported by the CSEDI program of the US National Science Foundation under grant EAR-0757871 and would not have been possible without the open availability of waveform data through the Data Management Center of the Incorporated Research Institutions for Seismology (IRIS).

References

Akaogi, M., Ito, E., Navrotsky, A., 1989. Olivine-modified spinelspinel transitions in the system Mg_2SiO_4–Fe_2SiO_4: calorimetric measurements, thermochemical calculations, and geophysical application. J. Geophys. Res. 94 (15), 671–685.

An, Y., Gu, Y.J., Sacchi, M.D., 2007. Imaging mantle discontinuities using least squares Radon transform. J. Geophys. Res. 112, doi:10.1029/2007JB005009, B10303.

Beylkin, G., 1985. Imaging of discontinuities in the inverse scattering problem by inversion of a causal generalized Radon transform. J. Math. Phys. 26, 99–108.

Bina, C.R., Wood, B.J., 1987. The olivine–spinel transitions: experimental and thermodynamic. Constraints and implications for the nature of the 400 km seismic discontinuity. J. Geophys. Res. 92, 4853–4866.

Bina, C.R., Helffrich, G., 1994. Phase transition Clapeyron slopes and transition zone seismic discontinuity topography. J. Geophys. Res. 99 (B8), 15853–15860.

Castle, J.C., Creager, K.C., 2000. Local sharpness and shear wave speed jump across the 660-km discontinuity. J. Geophys. Res. 105, 6191–6200.

Chaljub, E., Tarantola, A., 1997. Sensitivity of SS precursors to topography on the upper mantle 660-km discontinuity. Geophys. Res. Lett. 24, 2613–2616.

Chambers, K., Woodhouse, J.H., Deuss, A., 2005a. Reflectivity of the 410-km discontinuity from PP and SS precursors. J. Geophys. Res. 110, doi:10.1029/2004JB003345 (B02301).

Chambers, K., Woodhouse, J.H., Deuss, A., 2005b. Topography of the 410-km discontinuity from PP and SS precursors. Earth Planet. Sci. Lett. 235, 610–622.

Chambers, K., Woodhouse, J.H., 2006. Investigating the lowermost mantle using migrations of long-period S-ScS data. Geophys. J. Int. 166, 667–678.

Chapman, C.H., 1978. New method for computing synthetic seismograms. Geophys. J. Int. 54, 481–518.

Collier, J., Helffrich, G., 1997. Topography of the "410" and "660" km seismic discontinuities in the Izu-Bonin subduction zone. Geophys. Res. Lett. 24, 1535–1538.

Dahlen, F.A., Hungh, S.-H., Nolet, G., 2000. Fréchet kernels for finite-frequency travel times—I. Theory. Geophys. J. Int. 141, 175–203.

Dahlen, F.A., 2005. Finite-frequency sensitivity kernels for boundary topography perturbations. Geophys. J. Int. 162, 525–540.

De Hoop, M.V., Van der Hilst, R.D., 2005. On sensitivity kernels for wave equation transmission tomography. Geophys. J. Int. 160, doi:10.1111/j.1365-246X.2004.02509.

De Hoop, M.V., Van der Hilst, R.D., Shen, P., 2006. Wave-equation reflection tomography: annihilators and sensitivity kernels. Geophys. J. Int. 167, 1332–1352.

De Hoop, M.V., Smith, H., Uhlmann, G., Van der Hilst, R.D., 2009. Seismic imaging with the generalized Radon transform: a curvelet transform perspective. Inverse Problems 25, doi:10.1088/0266-5611/25/2/025005, 025005 (21 pp).

Deuss, A., Woodhouse, J.H., 2001. Seismic observations of splitting of the mid-transition zone discontinuity in earth's mantle. Science 294, 354–357.

Deuss, A., 2009. Global observations of mantle discontinuities using SS and PP precursors. Surv. Geophys. 30 (4–5), 301–326.

Deuss, A., Redfern, S.A.T., Chambers, K., Woodhouse, J.H., 2006. The nature of the 660-kilometer discontinuity in Earth's mantle from global seismic observations of PP precursors. Science 311, 198–201.

Engdahl, E.R., Van der Hilst, R.D., Buland, R.P., 1998. Global teleseismic Earthquake relocation from improved travel times and procedures for depth determination. Bull. Seis. Soc. Am. 88 (3), 722–743.

Fei, Y., van Orman, J., Li, J., van Westrenen, W., Sanloup, C., Minarik, W., Hirose, K., Komabayashi, T., Walter, M., Funakoshi, K., 2004. Experimentally determined postspinel transformation boundary in Mg_2SiO_4 using MgO as an internal pressure standard and its geophysical implications. J. Geophys. Res. 103, doi:10.1029/2003JB002562, B02305.

Flanagan, M.P., Shearer, P.M., 1998a. Global mapping of topography on transition zone velocity discontinuities by stacking SS precursors. J. Geophys. Res. 103, 2673–2692.

Flanagan, M.P., Shearer, P.M., 1998b. Topography on the 410-km seismic velocity discontinuity near subduction zones from stacking of sS, sP, and pP precursors. J. Geophys. Res. 103, 21165–21182.

Flanagan, M.P., Shearer, P.M., 1999. A map of topography on the 410-km discontinuity from PP precursors. Geophys. Res. Lett. 26, 549–552.

Frost, D.J., 2003. The structure and sharpness of $(Mg,Fe)_2SiO_4$ phase transformations in the transition zone. Earth Planet. Sci. Lett. 216, 313–328.

Gossler, J., Kind, R., 1996. Seismic evidence for very deep roots of continents. Earth Planet. Sci. Lett. 138 (1–4), 1–13.

Grand, S.P., 2002. Mantle shear-wave tomography and the fate of subducted slabs. Phil. Trans. R. Soc. Lond. A 360, 2475–2491.

Gu, Y.J., Dziewonski, A.M., Agee, C.B., 1998. Global de-correlation of the topography of transition zone discontinuities. Earth Planet. Sci. Lett. 157, 57–67.

Gu, Y.J., Dziewonski, A.M., 2002. Global variability of transition zone thickness. J. Geophys. Res. 107 (B7), doi:10.1029/2001JB000489.

Gu, Y.J., Dziewoński, A.M., Ekström, G., 2003. Simultaneous inversion for mantle shear velocity and topography of transition zone discontinuities. Geophys. J. Int. 154, 559–583.

Gu, Y.J., Sacchi, M., 2009. Radon transform methods and their applications in mapping mantle reflectivity structure. Surv. Geophys., doi:10.1007/s10712.009-9076-0.

Helffrich, G., 2000. Topography of the transition zone seismic discontinuities. Rev. Geophys. 38, 141–158.

Houser, C., Masters, G., Flanagan, M., et al., 2008. Determination and analysis of long-wavelength transition zone structure using SS precursors. Geophys. J. Int. 174 (1), 178–194.

Irifune, T., Isshiki, M., 1998. Iron partitioning in a pyrolite mantle and the nature of the 410-km seismic discontinuity. Nature 392, 702–705.

Ito, E., Takahashi, E., 1989. Postspinel transformations in the system Mg_2SiO_4–Fe·SiO_4 and some geophysical implications. J. Geophys. Res. 9, 10637–10646.

Jeanloz, R., Thompson, A.B., 1983. Phase transitions and mantle discontinuities. Rev. Geophys. 21, 51–74.

Katsura, T., Ito, E., 1989. The system Mg_2SiO_4–Fe_2SiO_4 at high pressures and temperatures: precise determination of stabilities of olivine, modified spinel, and spinel. J. Geophys. Res. 94, 15663–15670.

Kennett, B.L.N., Engdahl, E.R., Buland, R.P., 1995. Constraints on seismic velocities in the Earth from travel times. Geophys. J. Int. 122, 108–124.

Lawrence, J.F., Shearer, P.M., 2008. Imaging mantle transition zone thickness with SdS-SS finite-frequency sensitivity kernels. Geophys. J. Int. 174, 143–158.

Lebedev, S., Chevrot, S., van der Hilst, R.D., 2002. Seismic evidence for olivine phase change at the 410- and 660-kilometer discontinuities. Science 296, 1300–1302.

Lebedev, S., Chevrot, S., Van der Hilst, R.D., 2003. Correlation between the shear-speed structure and thickness of the mantle transition zone. Phys. Earth Planet. Int. 136, 25–40.

Li, B., Liebermann, R., 2007. Indoor seismology by probing the Earth's interior by using sound velocity measurements at high pressures and temperatures. Proc. Natl. Acad. Sci. 104, 9145–9150.

Ma, P., Wang, P., Tenorio, L., De Hoop, M.V., Van der Hilst, R.D., 2007. Imaging of structure at and near the core-mantle boundary using a generalized radon transform: 2. Statistical inference of singularities. J. Geophys. Res. 112, doi:10.1029/2006JB004513, B08303.

Miller, D., Oristaglio, M., Beylkin, G., 1987. A new slant on seismic imaging: migration and integral geometry. Geophysics 52, 943–964.

Neele, F., de Regt, H., Van Decar, J., 1997. Gross errors in upper-mantle discontinuity topography from underside reflection data. Geophys. J. Int. 129, 194–204.

Rigden, S.M., Gwanmesia, G.D., FitzGerald, J.D., Jackson, I., Liebermann, R.C., 1991. Spinel elasticity and seismic structure of the transition zone of the mantle. Nature 354, 143–145.

Ringwood, A.E., 1969. Phase transformations in the mantle. Earth Planet. Sci. Lett. 5, 401–412.

Ringwood, A.E., 1975. Composition and Petrology of the Earth's Mantle. McGraw-Hill, New York.

Ringwood, A.E., 1991. Phase transformations and their bearing on the constitution and dynamics of the mantle. Geochim. Cosmochim. Acta 55, 2083–2110.

Rondenay, S., Bostock, M.G., Fischer K.M., 2005. Multichannel inversion of scattered teleseismic body waves: practical considerations and applicability, in Seismic Earth: array analysis of broadband seismograms. In: Levander, A., Nolet, G. (Eds.), AGU Geophysical Monograph Series, 157.

Rost, S., Thomas, C., 2009. Improving seismic resolution through array processing techniques. Surveys in Geophysics 30 (4-5), 271–299.

Saikia, A., Frost, D., Rubie, D., 2008. Splitting of the 520-kilometer seismic discontinuity and chemical heterogeneity in the mantle. Science 319, 1515–1518.

Schmerr, N., Garnero, E., 2006. Investigation of upper mantle discontinuity structure beneath the central Pacific using SS precursors. J. Geophys. Res. 111, doi:10.1029/2005JB004197, B08305.

Shearer, P.M., 1990. Seismic imaging of upper-mantle structure with new evidence for a 520-km discontinuity. Nature 344, 121–126.

Shearer, P.M., 1991. Constraints on upper-mantle discontinuities from observations of long-period reflected and converted phases. J. Geophys. Res. 96, 18147–18182.

Shearer, P.M., Masters, T.G., 1992. Global mapping of topography on the 660-km discontinuity. Nature 355, 791–796.

Shearer, P.M., 1993. Global mapping of upper mantle reflectors from long-period SS precursors. Geophys. J. Int. 115, 878–904.

Shearer, P.M., 1996. Transition zone velocity gradients and the 520-km discontinuity. J. Geophys. Res. 101, 3053–3066.

Shearer, P.M., Flanagan, M.P., Hedlin, M.A.H., 1999. Experiments in migration processing of SS precursor data to image upper mantle discontinuity structure. J. Geophys. Res. 104, 7229–7242.

Shearer, P.M., 2000. Upper mantle seismic discontinuities, Earth's deep interior: mineral physics and tomography from the atomic to the global scale. Geophys. Monogr. 117, 115–131.

Shim, S.-H, Duffy, T.S., Shen, G., 2001. The post-spinel transformation in Mg_2SiO_4 and its relation to the 660-km seismic discontinuity. Nature 411, 571–574.

Spetzler, J., Snieder, R., 2004. The Fresnel volume and transmitted waves. Geophysics 69, 653–663.

Stixrude, L., Lithgow-Bertelloni, C., 2005. Mineralogy and elasticity of the upper mantle: origin of the low velocity zone. J. Geophys. Res. 110, doi:10.1029/2004JB002965, B03204.

Stolk, C.C., De Hoop, M.V., 2002. Microlocal analysis of seismic inverse scattering in anisotropic, elastic media. Commun. Pure Appl. Math. 55, 261–301.

Tromp, J., Tape, C., Liu, Q., 2005. Seismic tomography, adjoint methods, time reversal, and banana-donut kernels. Geophys. J. Int. 160, 195–216, doi:10.1111/j.1365-246X.2004.02456.x.

Van der Hilst, R.D., De, Hoop., Wang, M.V., Shim, S.-H., Tenorio, L., Ma, P., 2007. Seismo-stratigraphy and thermal structure of Earth's core-mantle boundary region. Science 315, 1813–1817.

Wang, P., de Hoop, M.V., van der Hilst, R.D., Ma, P., Tenorio, L., 2006. Generalized Radon transform imaging of the core mantle boundary: I—Construction of image gathers. Geophys. Res. 111, doi:10.1029/2005JB004241, B1230.

Wang, P., de Hoop, M.V., Van der Hilst, R.D., 2008. Imaging of the lowermost mantle (D″) and the core-mantle boundary with SKKS coda waves. Geophys. J. Int. 175, 103–115.

Weidner, D.J., Wang, Y.S., 2000. Phase transformations: implications for mantle structure. In: Karato et al. (Eds.), Earth's Deep Interior, Am. Geoph. Un., Geophys. Monogr., pp. 215–235.

Weidner, D., Li, L., Durham, W., Chen, J., 2005. In: Chen, J., et al. (Eds.), High-temperature Plasticity Measurements using Sychrotron X-rays. High-pressure Technology for Geophysical Applications. Elsevier Inc., San Diego, pp. 123–136.

Williams, Q., Revenaugh, J., 2005. Ancient subduction, mantle eclogite, and the 300 km seismic discontinuity. Geology 33, 1–4.

Woodland, A.B., Angel, R.J., 1997. Reversal of the orthoferrosilite-high-P clinoferrosilite transition, a phase diagram for $FeSiO_3$ and implications for the mineralogy of the Earth's upper mantle. Eur. J. Mineral. 9, 245–254.

Zhao, L., Chevrot, S., 2003. SS-wave sensitivity to upper mantle structure: implications for the mapping of transition zone discontinuity topographies. Geophys. Res. Lett. 30 (11), doi:10.1029/2003GL017223.

Zheng, Y., Lay, T., Flanagan, M.P., Williams, Q., 2007. Pervasive seismic wave reflectivity and metasomatism of the Tonga mantle wedge. Science 11, 855–859, 316, no. 5826.